Journal of Catalysis 279 (2011) 301–309

Contents lists available at ScienceDirect

Journal of Catalysis

journal homepage: www.elsevier.com/locate/jcat

A direct sulfation method for introducing the transition metal cation Co^{2+} into ZrO_2 with little change in the Brønsted acid sites

Xiangjie Wang, Huayu Wang, Yongchun Liu, Fudong Liu, Yunbo Yu *, Hong He *

State Key Laboratory of Environmental Chemistry and Ecotoxicology, Research Center for Eco-environmental Sciences, Chinese Academy of Sciences, 18 Shuangqing Road, Haidian District, Beijing 100085, China

ARTICLE INFO

Article history:
Received 12 November 2010
Revised 24 January 2011
Accepted 25 January 2011

Keywords:
Sulfation
Solid acid
Selective catalytic reduction
Solid solution

ABSTRACT

Direct sulfation of Zr–Co hydroxides provides a significant advantage over traditional impregnation by conserving Brønsted acid sites for the introduction of a second active component and also for subsequent catalytic reactions. After Pd loading, sulfated Zr–Co exhibits excellent activity, selectivity, and durability for the selective catalytic reduction of NO_x by methane. Using Co *K*-edge X-ray absorption spectroscopy, we provide the direct evidence of the entrance of Co into the lattice of cubic zirconia to form a substitutional solid solution.

© 2011 Elsevier Inc. All rights reserved.

1. Introduction

Sulfated metal oxides with both Brønsted and Lewis acid sites are widely used as solid acid catalysts and/or supports in organic synthesis, transformation reactions, and NO_x removal [1–7]. Of particular interest is sulfated zirconia, which possesses more acid sites than other sulfated metal oxides [8–13]. Zirconia exists in several crystalline forms: monoclinic, tetragonal, and cubic. It exists mainly in the tetragonal phase in the presence of S [14,15]. Using periodic ab initio calculations, Haase and Sauer [16] suggested that the most stable configurations of sulfur species on the surface of tetragonal zirconia are the tridentate sulfate anion and the $-SO_3$ complex. Details of the type and number of acid sites on sulfated zirconia have been identified by ^{13}C NMR, ^{31}P NMR, and pyridine adsorption [17–19]. To further improve the properties of sulfated zirconia, active component transition metal cations have been introduced into sulfated zirconia by impregnation. Li et al. [19,20] reported that the loading of Co over sulfated zirconia exhibits high activity for the selective catalytic reduction of NO_x by methane. Mn^{2+} and Fe^{3+} show significant catalytic effects on *n*-butane isomerization over sulfated zirconia [21–25]. Arata and co-workers [26] reported that Pt-added sulfated zirconia was active for the dehydrogenative coupling of methane. However, this conventional impregnation method often decreases the number of Brønsted acid sites, since these sites are preferentially occupied by the cations introduced, such as Co [19] and Pd [27,28]. As Brønsted acid sites play a crucial role both in anchoring other active components and in catalytic reactions [29–31], such a decrease would cause deterioration in the intrinsic properties of solid acid materials. Thus, designing and implementing new methods for the introduction of transition metals into sulfated zirconia while minimizing the consumption of Brønsted acid sites is of particular importance.

In the present study, the selective catalytic reduction of NO_x by methane (CH_4-SCR) was used as a probe reaction because the number of Brønsted acid sites is very important for this reaction [32–38]. Sulfated zirconia is commonly used as a support for catalysts used in CH_4-SCR [39–47]. Both Co^{2+} and Pd^{2+} are further introduced into sulfated zirconia to enhance its activity and durability [39,40,42,43]. The Co species in previous studies were introduced by impregnation at the expense of Brønsted acid sites. Thus, it is important to find a new method of introducing Co^{2+} into zirconia with little change in the Brønsted acid sites. Here, the direct sulfation of Zr–Co hydroxides is employed to introduce Co species. The number of Brønsted acid sites on sulfated Zr–Co oxide (denoted as SZC) prepared by this method was much larger than that on zirconia prepared by the impregnation method. As a result, sufficient Brønsted acid sites are left available for the introduction of a second active component and subsequent catalytic reactions. Specifically, a SZC-supported Pd catalyst (PdSZC) was further prepared by the impregnation method. As expected, PdSZC showed high activity toward CH_4-SCR.

* Corresponding authors. Fax: +86 10 6284 9121.
E-mail addresses: ybyu@rcees.ac.cn (Y. Yu), honghe@rcees.ac.cn (H. He).

0021-9517/$ - see front matter © 2011 Elsevier Inc. All rights reserved.
doi:10.1016/j.jcat.2011.01.026

2. Experimental

2.1. Catalyst preparation

The Zr–Co hydroxides were prepared by the co-precipitation method using a mixture of aqueous solutions of $Zr(NO_3)_4$ and $Co(NO_3)_2$ (Zr:Co = 9:1 mol ratio) and $NH_3{\cdot}H_2O$ (26 wt.%) as the precipitator to maintain a pH of 9. The precipitate was washed thoroughly and then dried at 120 °C for 12 h. Subsequently, SZC samples with different S loadings were obtained by immersing the above hydroxides into a 0.5 M $(NH_4)_2SO_4$ solution, drying them over a water bath at 60 °C, and then calcining them at 550 °C for 3 h in air in sequence. Sulfated zirconia with 2 wt.% S (SZ) was also prepared according to the above steps. The PdSZC sample (0.2 wt.% Pd) was prepared by immersing SZC (with 2 wt.% S) in a $Pd(NO_3)_2$ solution using steps similar to those followed for the preparation of SZC. SZ-supported Co (CoSZ, 4 wt.% Co), SZ-supported Pd (PdSZ, 0.2 wt.% Pd), and CoSZ-supported Pd (PdCoSZ, 0.2 wt.% Pd) were prepared by the impregnation method for use as reference materials.

2.2. Catalytic activity tests

The activity tests were carried out in a fixed bed quartz tube reactor over a temperature range of 250–500 °C. Approximately 1.2 ml (1.7 g) of the catalyst sample (40–60 mesh) was used, and the reaction conditions were 1500 ppm CH_4, 500 ppm NO, 7.5 vol.% O_2, N_2 balanced, 200 ml min^{-1} total flow rate, and GHSV = 10,000 h^{-1} (or 3600 h^{-1}, 3.3 ml catalyst). Durability tests of PdSZ and PdSZC for CH_4-SCR were carried out at 460 °C under the same conditions. The concentrations of NO, NO_2, N_2O, and CH_4 in the inlet and outlet streams were measured by an online Nicolet 380-FTIR spectrometer equipped with a gas cell of volume 0.2 dm^3. To measure the mass balance of nitrogen during the CH_4-SCR reaction over PdSZC, the reaction gas mixture was balanced by Ar, and an online gas chromatograph (SHIMDZU GC 2014C) equipped with a TCD detector was used to monitor the formation of N_2. A molecular sieve column (MS-13X) was used to separate O_2 and N_2 at 24 °C. Based on the experiment, we can calculate the nitrogen balance (inlet ($[NO] + [NO_2]$) = outlet ($[NO] + [NO_2] + [N_2O] + [N_2]$)). Over PdSZC, the nitrogen balance was higher than 97%. The turnover frequency (TOF) was calculated according to the molar ratio of N_2 produced per second to Pd.

2.3. Catalyst characterization

BET (Brunauer, Emmett, and Teller) surface areas and pore diameter distributions were obtained from N_2 adsorption and desorption at 77 K on Quantasorb-18 automatic equipment (Quanta Chrome Instrument Co.). Before the measurements were obtained, all samples were first evacuated at 80 °C for 0.5 h and then raised to 300 °C and kept for 5 h. The elemental compositions of the powder catalysts were determined by a sequential X-ray fluorescence spectrometer (XRF-1800, Shimadzu).

The diffuse reflectance infrared Fourier transform spectroscopy (DRIFTS) spectra of pyridine adsorption on different samples were recorded on a FTIR spectrometer (Thermo Nicolet Corporation Nexus 670, OMNIC Quantpad software) equipped with a smart collector and a MCT/A detector cooled by liquid nitrogen. The reaction temperature was controlled by an Omega programmable temperature controller. The sample was finely ground and then placed in a ceramic crucible in an in situ chamber. Prior to pyridine adsorption, the sample was pretreated at 500 °C in a flow of 20 vol.% O_2 + 80 vol.% N_2 at a rate of 100 ml min^{-1} for 30 min and then cooled to the desired temperatures (300 and 30 °C) to obtain a reference spectrum. The sample was then exposed to saturated pyridine vapor at 30 °C for 20 min, after which the DRIFTS spectra of pyridine adsorption were recorded. All reported spectra were taken at a resolution of 4 cm^{-1} for 100 scans.

Powder X-ray diffraction (XRD) analysis was carried out on an XPERT-PRO diffractometer system operated at an accelerating voltage of 40 kV and an emission current of 40 mA with Cu $K\alpha$ radiation (λ = 1.540598 Å). Data were acquired over the range of 20–90° 2θ with a step rate of 4° min^{-1}.

Raman spectra were obtained at room temperature with a UVR DLPC-DL-03 UV resonance Raman spectrometer equipped with a CCD detector cooled with liquid N_2. The instrument was calibrated against the Stokes Raman signal of Teflon at 1378 cm^{-1}. A continuous He–Ne laser beam (325 nm) was used as the exciting radiation, and a source power of 5 mW was used. The spectral resolution was 2.0 cm^{-1}.

Zr *K*-edge X-ray absorption spectroscopy (XAS) was measured at the 1W1B-XAFS beam line at the Beijing Synchrotron Radiation Facility (BSRF). The storage ring was operated at 2.5 GeV and 200 mA. The spectra were collected at room temperature in transmission mode. Co *K*-edge XAS was performed at the BL14W1-XAFS beam line at the Shanghai Synchrotron Radiation Facility (SSRF). Here, the storage ring was operated at 3.5 GeV and 200 mA. The spectra were collected at room temperature in fluorescence mode with an energy resolution of 0.3 eV. The reduction and analysis of all spectra were performed using the methods of Athena and Artemis from the ifeffit1.2.11c software package [48], which was further fitted in R-space with theoretical models constructed based on the crystal structure of SZC samples from FEFF8 [49]. The *k* values used to fit the Zr *K*-edge ranged from 2 to 12; the range from 2 to 10.2 was used to fit the Co *K*-edge.

H_2 temperature-programmed reduction (H_2-TPR) experiments were carried out with a H_2/Ar (4.79 vol.%) flow of 40 ml min^{-1} from 50 to 700 °C with a ramp of 10 °C min^{-1}. Before the TPR experiments, all samples were pretreated in an O_2 atmosphere at 500 °C for 1 h. H_2 consumption was determined by mass spectrometry (Hiden HPR 20), and the production of SO_2, H_2S, and H_2O was simultaneously determined.

3. Results

3.1. BET measurement and elemental composition analysis

The BET-specific surface area, pore volume, and mean pore diameter of the catalysts are summarized in Table 1. It is clear that sulfation increased the surface area of the SZC samples. The BET-specific surface area of SZC (3 wt.% S) is 121 m^2/g, nearly twice that of SZC without S. The pore volumes of SZC changed slightly with increasing S loading. However, the mean pore diameter of SZC decreased gradually with increasing S content. CoSZ, PdCoSZ, and PdSZC exhibited similar surface areas; the PdSZ catalyst showed the largest surface area among the samples.

Table 1
Physical properties of different samples.

Sample	S_{BET} (m^2/g)	Pore volume (cc/g)	Mean pore diameter (nm)	Elemental composition (wt.%)[a]		
				S	Co	Zr
SZC 0 wt.% *S*	64	0.094	5.9	0	4.10	68.0
SZC 1 wt.% *S*	89	0.088	3.9	0.97	4.01	66.7
SZC 2 wt.% *S*	90	0.078	3.5	2.08	3.97	65.9
SZC 3 wt.% *S*	121	0.084	3.5	2.96	3.97	65.4
SZ	106	0.092	3.5	1.97	0	70.0
CoSZ	100	0.086	3.4	1.97	4.22	65.7
PdSZ	117	0.108	3.7	1.88	0	70.3
PdCoSZ	100	0.077	3.1	1.79	3.87	66.4
PdSZC	99	0.083	3.3	2.13	4.21	65.7

[a] Measured by XRF.

The elemental compositions of the SZ, CoSZ, SZC, and Pd-added catalysts were measured by XRF, with the results shown in Table 1. Clearly, the S and Co content in all samples was almost identical to the corresponding nominal values. This proves that the two species do not dissolve into the aqueous solution during the sequential immersion process. The Pd species was not detected by XRF, likely due to its low concentration (0.2 wt.%).

3.2. Pyridine adsorption experiment

Pyridine adsorption was used to determine the acid sites and the acidity on SZC samples with different S loadings (Fig. 1a). The bands at 1439 and 1541 cm^{-1} were attributed to the characteristics of adsorbed pyridine bound to Lewis and Brønsted acid sites, respectively [19]. The Brønsted acid sites on the SZC samples increased perceptibly as the S content increased from 0 to 2 wt.%, but they decreased when the S content was further increased to 3 wt.%. Meanwhile, the Lewis acid sites increased significantly with S addition. The same pyridine adsorption experiment was also performed on SZ, CoSZ, PdSZC, and PdCoSZ samples (Fig. 1b). The number of Brønsted acid sites on SZC was larger than that on CoSZ with the same Co and S content. In comparison with SZC (with 2 wt.% S), the Brønsted acid sites on the PdSZC catalyst decreased sharply. This trend shows that the introduction of Pd consumes Brønsted acid sites. In other words, Pd species with the form Pd^{2+} are anchored to Brønsted acid sites [27,28,33,34]. Pd species in the PdCoSZ catalyst were difficult to anchor onto Brønsted acid sites, considering that the Brønsted acid sites in CoSZ hardly changed with Pd introduction. In PdCoSZ, Pd may exist in the form of PdO. To examine the strength of Brønsted acids, samples were heated from 30 to 300 °C under N_2 flow after pyridine adsorption. The SZC sample with 2 wt.% S maintained nearly the same Brønsted acidity as SZ, which was also more abundant than that of CoSZ (Fig. 2b). Thus, we successfully developed a new method for the introduction of Co into ZrO_2 with little change in the number of Brønsted acid sites. A peak at 1444 cm^{-1} was observed for all Co-containing samples in Fig. 1b; this peak was assigned to the Lewis acid sites related to Co species that were anchored to the Brønsted sites formed by sulfation.

3.3. XRD characterization

The XRD patterns of SZC with different S content and SZ are shown in Fig. 3. SZ featured the typical tetragonal phase of zirconia (ICSD 070014). It is well known that surface sites, which adsorb oxygen at low temperatures, are responsible for causing the tetragonal phase to undergo monoclinic transformation at low temperatures; in contrast, the incorporation of sulfate covers these sites and maintains the tetragonal phase [15]. After the introduction of Co via traditional impregnation, tetragonal ZrO_2 species in the SZ sample were also retained. In this case, the Co species was present as Co_3O_4. In contrast to the SZ sample, shoulder peaks at 34.7°

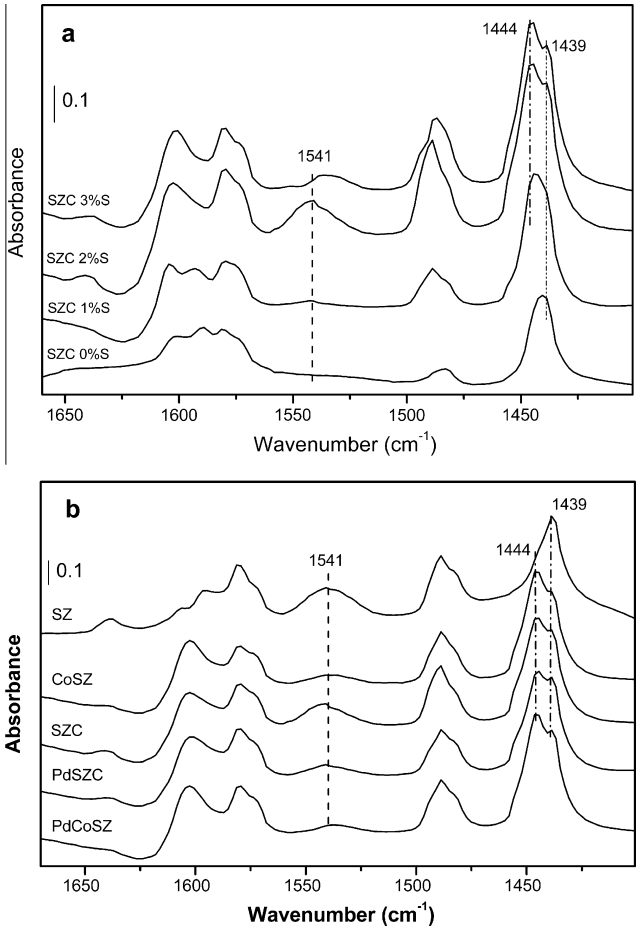

Fig. 1. DRIFT spectra of pyridine adsorption at 30 °C over (a) SZC with different S loadings; (b) samples containing 2 wt.% S prepared by direct sulfation and traditional impregnation methods.

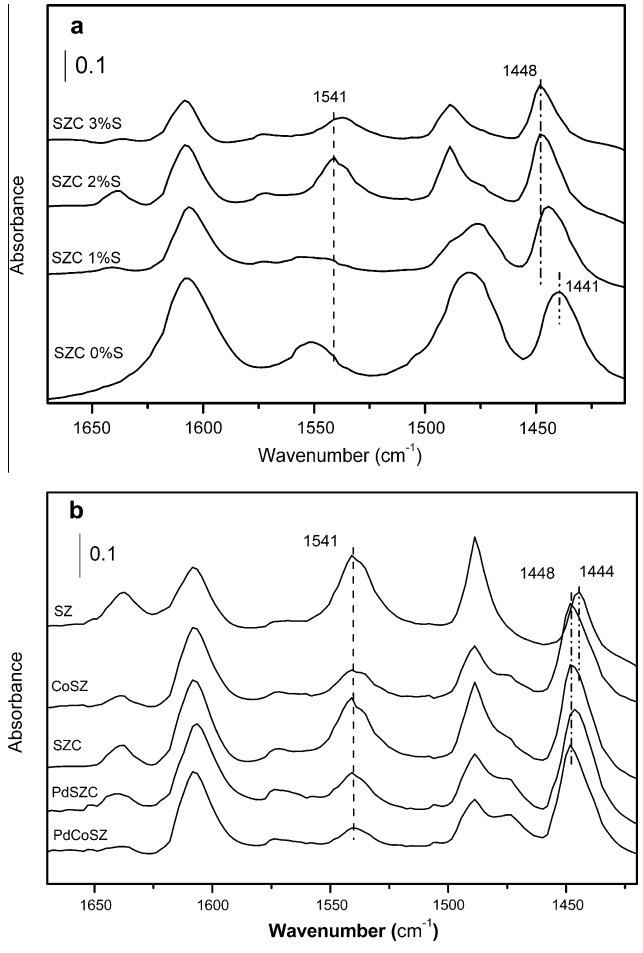

Fig. 2. DRIFT spectra of (a) SZC with different S loadings; (b) samples containing 2 wt.% S prepared by direct sulfation and traditional impregnation methods after exposed to saturated pyridine vapor at 30 °C and then purged in N_2 for 20 min at 300 °C.

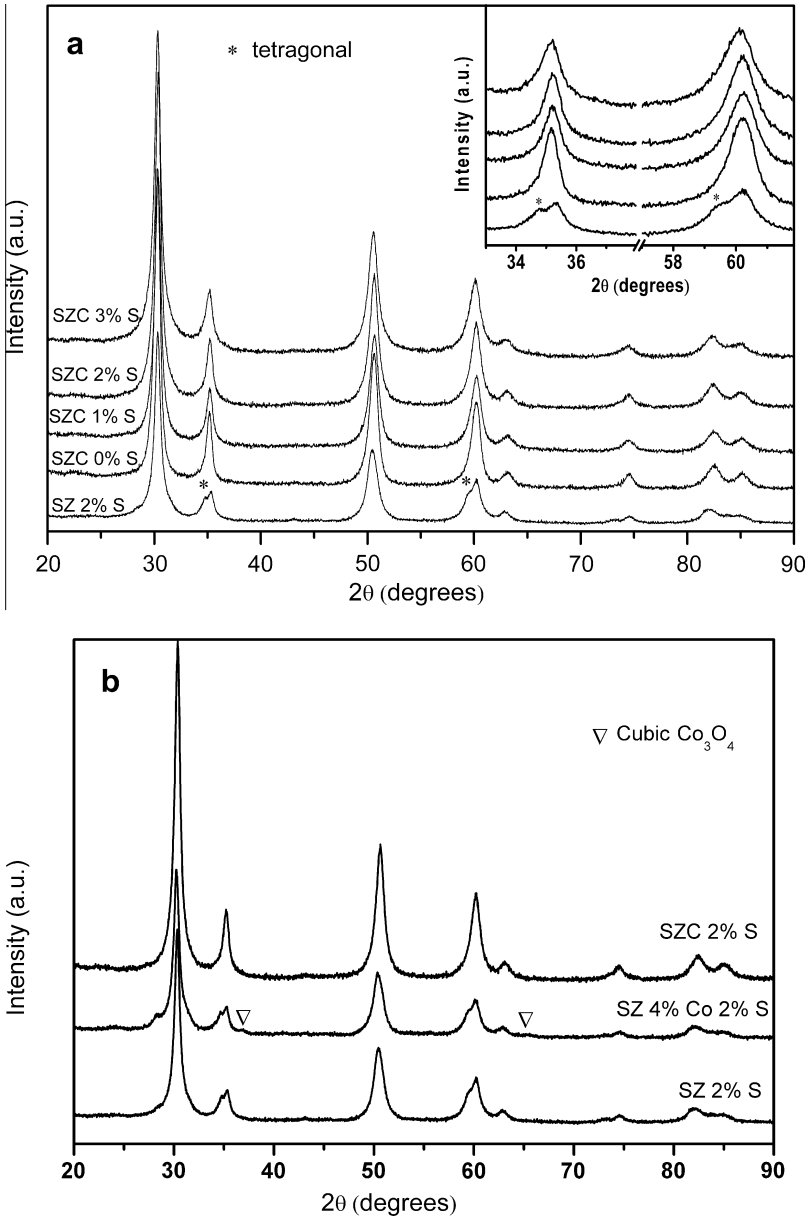

Fig. 3. (a) XRD patterns of SZ and SZC with different S loadings; (b) XRD patterns of SZ, CoSZ, and SZC with 2 wt.% S.

(0 0 2) and 59.5° (1 0 3) disappeared obviously in the SZC samples, strongly suggesting that phase transformation occurred due to the addition of Co and that a cubic phase may be present in the SZC samples (ICSD 072955).

To examine the index and identify the phase of the samples, XRD pattern refinement with GSAS was performed using EXPGUI software [50], the results of which are shown in Table 2. The cubic phase was present in the SZC samples, with lattice constants rising slowly from 5.100004 to 5.106705 Å with increasing S loading.

Table 2
Determination of crystalline phase (cubic or tetragonal) of SZC samples with different S content and SZ from X-ray diffraction analysis. EXPGUI software of GSAS (General Structure Analysis System) was used.

Sample	Crystalline phase	Lattice constant (Å)	R_p (%)	R_{wp} (%)	R (F^2) (%)
SZC 0 wt.% *S*	Cubic[a]	*a* = 5.100004	2.22	2.89	2.01
SZC 1 wt.% *S*	Cubic[a]	*a* = 5.104160	2.17	3.23	2.75
SZC 2 wt.% *S*	Cubic[a]	*a* = 5.105236	2.11	2.86	3.80
SZC 3 wt.% *S*	Cubic[a]	*a* = 5.106705	2.89	5.19	1.65
SZ 2 wt.% *S*	Tetragonal[b]	*a* = 3.599640 *b* = 5.180907	2.78	3.82	2.92

[a] Space group *f m* 3 *m*.
[b] Space group *P* 42/*n m c*.

3.4. Raman characterization

The Raman spectra of SZ and SZC are shown in Fig. 4. The Raman bands of SZ were located at 262, 307, 451, and 636 cm^{-1}, all of which are characteristic of the typical tetragonal phase [24,51]. SZC, however, showed no such bands. The XRD results confirm that SZ samples exist in the tetragonal phase, and a phase transformation occurs in SZC samples due to the addition of Co into zirconia.

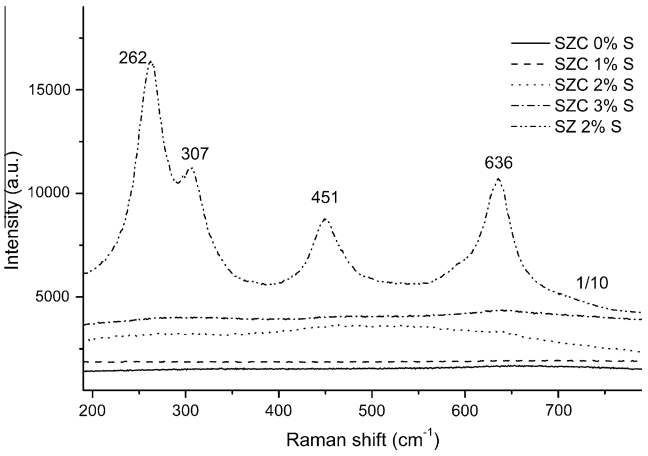

Fig. 4. Raman shift of SZ and SZC with different S loadings.

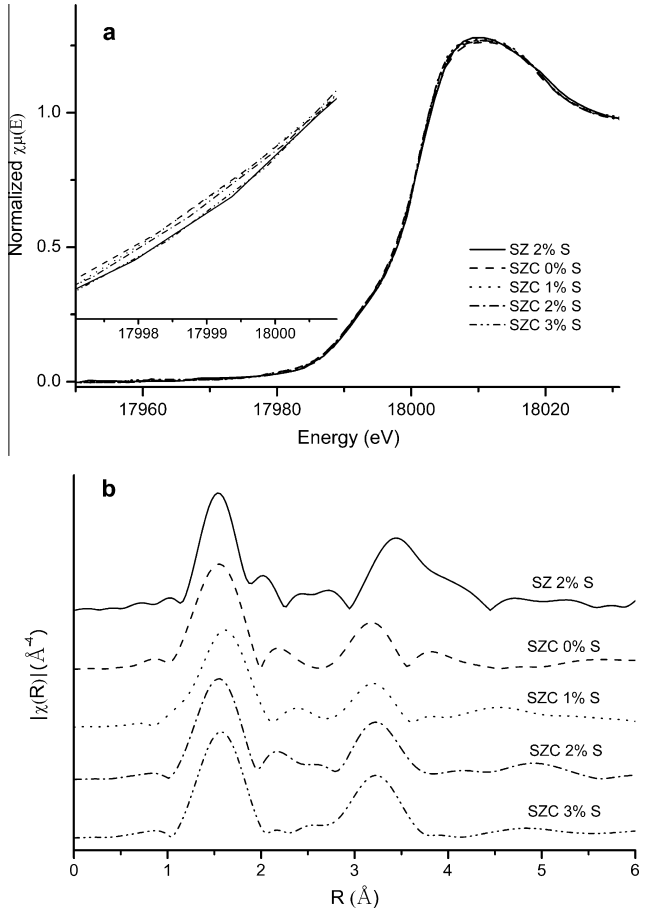

Fig. 5. (a) Zr *K*-edge XANES of SZ and SZC with different S loadings; (b) Fourier transforms of k^3-weighted EXAFS oscillation of Zr *K*-edge of SZ and SZC with different S loadings (sin window function covering the *k* range of 2–12 $Å^{-1}$ was used).

3.5. XAS measurements

3.5.1. XAS for the Zr K-edge

Fig. 5a shows the Zr *K*-edge XANES spectra of SZ and SZC with different S loadings. The XANES spectra of all samples are very similar, and their half-height edge positions shift to higher energies with increasing S loading, as shown in the inset of Fig. 5a.

The Fourier transform (k^3, $2.0 < k < 12.0$) EXAFS for the Zr *K*-edge of SZC and SZ are shown in Fig. 5b. The Fourier transforms of SZC with different S loadings vary minimally compared to the SZ sample. To obtain additional information, curve-fitting analysis of EXAFS data was performed. In this case, the cubic phase was selected as a model phase. The lattice constant used for this phase is listed in Table 2. For the EXAFS simulations, complex backscattering amplitudes were calculated using FEFF 8; the S_0 value of the Zr *K*-edge, as an amplitude reduction factor, was fixed at 0.66 according to the tetragonal ZrO_2 material model, thereby facilitating the correct determination of the coordination numbers. The fitting results of the first and second shells were listed in Tables 3 and 4. The results of cubic phase fitting are reasonable, further confirming that the zirconia in SZC samples mainly exists in cubic phase.

3.5.2. XAS for the Co K-edge

No information about Co species was obtained from the XRD results of SZC. There are two possible reasons for this: (1) Co could have formed an interstitial or substitutional solid solution with zirconia; or (2) Co could have been isolated and highly dispersed in the samples. To determine the state of Co species in the SZC samples, Co *K*-edge XAS was performed at room temperature. As shown in Fig. 6a, the pre-edge peak at ca. 7710 eV was ascribed to the 1*s* 3*d*-e.g. transition of Co *K* in the SZC samples [52]. The half-height edge positions of SZC were close to that of $Co(NO_3)_2$, but there were 4 eV lower than that of Co_3O_4, indicating that Co species in the SZC samples are mainly present as Co^{2+}. It can be seen from Fig. 6a that the S content (0–2 wt.%) had little effect on the Co state. When the S content was 3 wt.%, the Co *K*-edge absorption energy at half-height shifted to a higher value, with a shoulder peak at 7731 eV, indicating the formation of Co_3O_4 (Fig. 6a).

The Fourier transform of k^3-weighted EXAFS oscillations for the Co *K*-edge of SZC and Co_3O_4 are shown in Fig. 6b. The SZC samples with S content from 0 to 2 wt.% showed the same Co–O bond length; however, the SZC sample with 3 wt.% S loading exhibited a Co–O bond length similar to that of the Co_3O_4 species. These results further confirm the formation of Co_3O_4 species in SZC when the S content is 3 wt.%.

In Fig. 6b, a second coordination shell was observed for the SZC 0 wt.% S sample; this requires further verification. Therefore, the EXAFS spectrum of this sample was fitted with the assumption that Co is present in one of the following phases: cubic CoO (a = 4.2495 Å), substitutional solid solution in cubic zirconia, or interstitial solid solution in cubic zirconia. For the Co *K*-edge EXAFS simulations, complex backscattering amplitudes were also calculated using FEFF 8; the S_0 value of the Co *K*-edge was fixed at 1, according to the model material of Co_3O_4, which facilitated the correct determination of the

Table 3
The EXAFS fitting results of different S loading samples at the Zr *k* edge for the first shell. Sin window function covering the *k* range 2.0–12.0 $Å^{-1}$ was used.

Sample	Shell	CN[a]	R[b] (Å)	σ^{2c} (10^{-3} $Å^2$)	ΔE (eV)	ΔR (Å)	R factor (%)
SZC 0 wt.% S	Zr–O	6.8 ± 1.8	2.11 ± 0.02	7.0 ± 2.0	−12.9 ± 3.6	1.0–2.1	8.5
SZC 1 wt.% S	Zr–O	7.2 ± 0.9	2.15 ± 0.01	8.2 ± 1.3	−9.4 ± 1.7	1.0–2.1	2.1
SZC 2 wt.% S	Zr–O	6.8 ± 2.2	2.10 ± 0.02	7.8 ± 3.2	−13.4 ± 4.6	1.0–2.1	10.8
SZC 3 wt.% S	Zr–O	7.7 ± 1.2	2.11 ± 0.01	8.0 ± 1.5	−12.9 ± 2.2	1.0–2.1	1.94

[a] CN: coordination number.
[b] *R*: bond distance.
[c] σ^2: Debye–Waller factor.

Table 4
The EXAFS fitting results of different S loading samples at the Zr *k* edge for the second shell. Sin window function covering the *k* range 2.0–12.0 Å^{-1} was used.

Sample	Shell	CN[a]	R[b] (Å)	σ^{2}[c] (10^{-3} Å^2)	ΔE (eV)	ΔR (Å)	R factor (%)
SZC 0 wt.% S	Zr–Zr	6.5 ± 5.5	3.58 ± 0.04	1.8 ± 0.7	−9.0 ± 4.8	1.0–3.7	8.5
SZC 1 wt.% S	Zr–Zr	10.5 ± 6.0	3.60 ± 0.02	2.3 ± 0.4	−8.0 ± 2.1	1.0–3.7	2.1
SZC 2 wt.% S	Zr–Zr	3.9 ± 3.1	3.63 ± 0.04	1.3 ± 0.6	−3.6 ± 5.6	1.0–3.7	10.8
SZC 3 wt.% S	Zr–Zr	6.1 ± 1.9	3.61 ± 0.02	1.5 ± 0.2	−5.3 ± 2.0	1.0–3.7	1.9

[a] CN: coordination number.
[b] R: bond distance.
[c] σ^2: Debye–Waller factor.

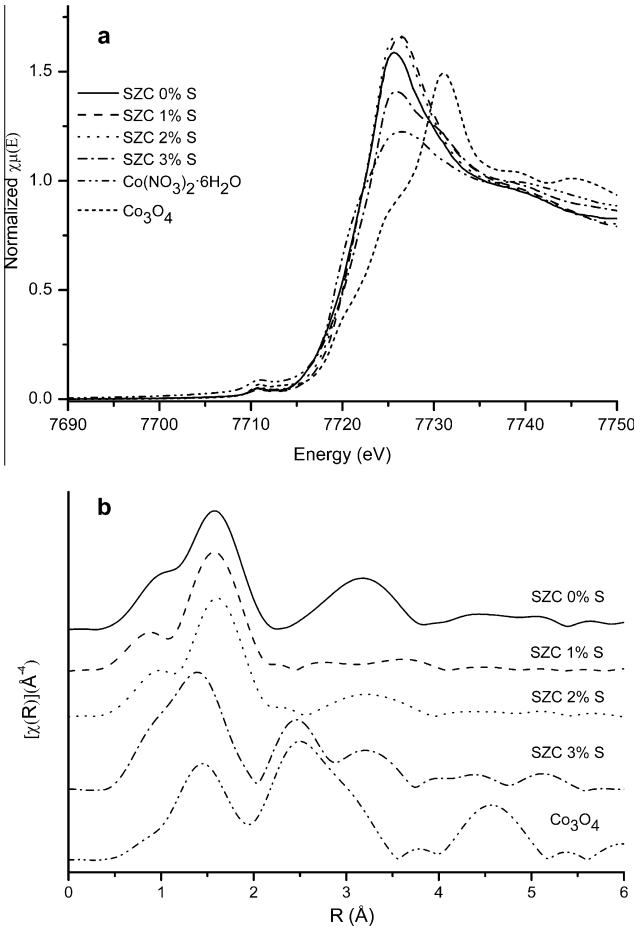

Fig. 6. (a) Co *K*-edge XANES of Co_3O_4, $Co(NO_3)_2{\cdot}6H_2O$ and SZC with different S loadings; (b) Fourier transforms of k^3-weighted EXAFS oscillation of Co *K*-edge of Co_3O_4 and SZC with different S loadings (sin window function covering the *k* range of 2–10.2 Å^{-1} was used).

coordination number. Fitting results demonstrate that isomorphous substitution of Co in cubic zirconia is reasonable (Tables 5 and 6, Fig. 7). To the best of our knowledge, this is the first time that evidence of Co entering the lattice of cubic zirconia to form a substitution solid solution was provided. The second coordination shell of SZC with 3 wt.% S was similar to that of the referential Co_3O_4 material, also confirming the formation of Co_3O_4.

3.6. Activity test

The catalysts were tested for CH_4-SCR, and the results of which are shown in Fig. 8. Fig. 8a depicts the activity of SZC samples at a low space velocity of 3600 h^{-1}. Obviously, the S content has a great influence on the activity of SZC during NO_x reduction. Increasing the S loading from 0 to 2 wt.% significantly increased NO_x conversion to

Table 5
The EXAFS fitting results of SZC with 0 wt.% S sample at the Co *K* edge for the first and second shells. Sin window function covering the *k* range 2.0–10.2 Å^{-1} was used.

Shell	Atom	CN[a]	R (Å)[b]	R_0 (Å)[c]	R factor (%)
1	O	7.0 ± 1.2	2.18	2.21	2.1
2	Zr	12.7 ± 5.6	3.59	3.61	2.8

[a] CN: coordination number.
[b] R: bond distance fitted.
[c] R_0: bond distance calculated.

N_2, while further increases in S content to 3 wt.% decreased such activity. The SZC with 2 wt.% S was used for the introduction of a second active species of Pd. The following activity tests were preformed at a high space velocity of 10,000 h^{-1}. As shown in Fig. 8b, CoSZ prepared by the traditional impregnation method showed marginal activity for NO_x reduction within the temperature region 250–500 °C, while SZC with 2 wt.% S provided ca. 20% NO_x conversion to N_2 at above 400 °C. After the second active component of Pd was introduced into SZC (PdSZC), NO_x conversion to N_2 increased to 82%, three times higher than that of SZC. For PdCoSZ, however, the conversion of NO_x was below 26% in the temperature range 250–500 °C. The TOFs of the PdSZC and PdCoSZ catalysts for NO_x reduction were calculated based on the data at 450 °C. At this temperature, the former exhibits a TOF value of 1.4×10^{-3} s^{-1}, 2.2 times higher than that of the latter catalyst (4.4×10^{-4} s^{-1}).

N_2O as a main byproduct was commonly observed during the SCR of NO_x [53]; this byproduct was also detected during NO_x reduction by CH_4 [45,54]. During NO_x reduction by methane over PdSZ, large amounts of N_2O were formed above 400 °C. Interestingly, PdSZC significantly lowered the formation of N_2O compared to PdSZ (Fig. 8c), indicating that the introduction of Co enhanced selectivity to N_2 during CH_4-SCR.

The PdSZC catalyst exhibited much greater durability than PdCoSZ, maintaining ca. 84% NO_x conversion to N_2 at 460 °C until 35 h; in contrast, the latter material showed a gradual decrease in NO_x conversion under the same reaction conditions (Fig. 8d). The durability of the PdSZC catalyst for NO_x reduction was also evaluated in the presence of 10% water vapor; the results are shown in Fig. 8d. At 500 °C, NO_x conversion to N_2 decreased from 80% to 60% after 6.4 h, indicating that the water tolerance of this catalyst requires improvement in future research.

3.7. TPR

Resasco and co-workers [25] reported that the state of Pd plays a crucial role in the activity of SZ-supported catalysts. To further confirm this, H_2-TPR experiments were performed, and the results of which are shown in Fig. 9. H_2 consumption was observed between 100 and 200 °C for PdCoSZ, which can be attributed to PdO species [55]. The PdSZC sample showed no H_2 consumption over the same temperature range, indicating that Pd^{2+} was tightly

Table 6
The EXAFS fitting results of SZC with S loading from 0 to 3 wt.% at the Co *K* edge for the first shell. Sin window function covering the *k* range 2.0–10.2 Å^{-1} was used.

Sample	Shell	CN[a]	*R*[b] (Å)	σ^{2c} (10^{-3} Å^2)	ΔE (eV)	ΔR (Å)	*R* factor (%)
SZC 0 wt.% S	Co–O	7.0 ± 1.2	2.18 ± 0.01	12.0 ± 2.0	−21.2 ± 2.1	0.6–2.3	1.6
SZC 1 wt.% S	Co–O	7.9 ± 1.2	2.19 ± 0.01	9.0 ± 1.7	−20.2 ± 1.9	0.6–2.3	1.3
SZC 2 wt.% S	Co–O	7.7 ± 1.6	2.20 ± 0.02	9.8 ± 2.3	−19.0 ± 2.6	0.6–2.3	2.5
SZC 3 wt.% S	Co–O	5.7 ± 0.7	1.95 ± 0.04	20.5 ± 2.8	−8.5 ± 5.9	0.6–2.3	8.3

[a] CN: coordination number.
[b] *R*: bond distance.
[c] σ^2: Debye–Waller factor.

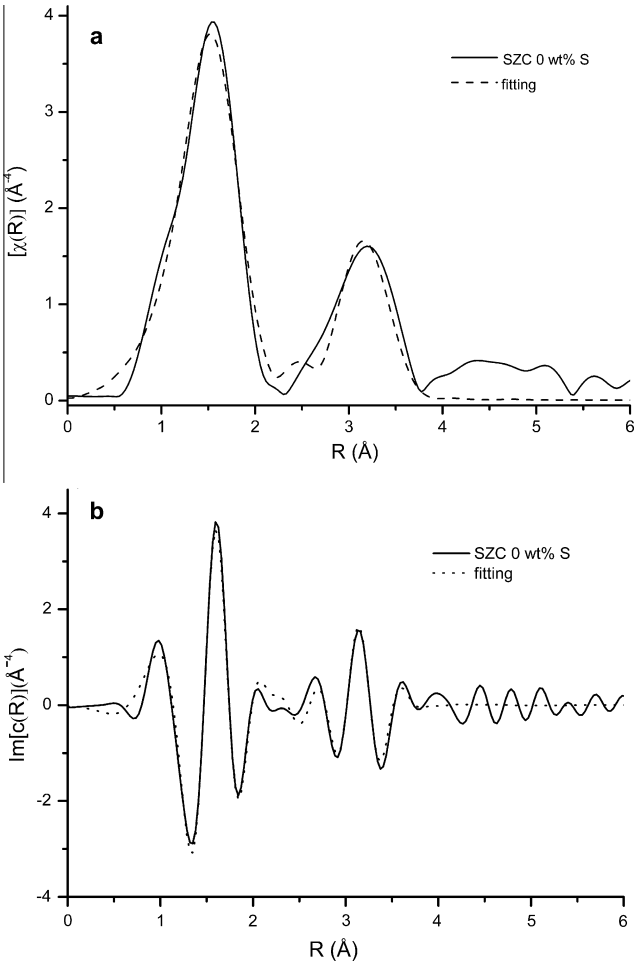

Fig. 7. Fourier transforms of Co *K*-edge k^3-weighted EXAFS spectra of SZC with 0 wt.% S (Full line, experimental; dashed line, fitting). (a) *R*-space; (b) real part in *R*-space.

bonded to and highly dispersed onto SZC without the formation of PdO species [55].

4. Discussion

4.1. Structure analysis of sulfated Zr–Co materials

The XRD, Raman, and Zr and Co *K*-edge XAS data confirm that the Zr–Co solid solution was present in the cubic phase, and this structure did not change as long as the S loading remained below 3 wt.%. Further increasing the S content to 3 wt.% resulted in the formation of the Co_3O_4 phase (Fig. 6 and Table 6). To verify this observation, the concentration of S species on the surface of ZSC was calculated.

As suggested by Xia and co-workers [56], the (1 1 1) surface of cubic zirconia is energetically favorable, and its stability is closely equivalent to that of the (1 0 1) surface of tetragonal zirconia [57]. On the latter surface, Haase and Sauer [16] proved that the most stable configuration of sulfur species adsorbed onto Zr sites is the tridentate sulfate anion. When the S content was increased from 0 to 2 wt.%, Zr *K*-edge XANES shifted to higher energy (Fig. 5a), while the energy of Co *K*-edge XANES (Fig. 6b) hardly changed with increasing S content. This suggests the direct coordination of Zr atoms to strongly electron-withdrawing SO_x centers [58]. Keeping this in mind, tridentate sulfate anions adsorbed onto Zr sites were employed in our calculations. Katada et al. adopted an ingenious way to estimate the surface area occupied by one sulfate anion [59]. Inspired by this, we calculated S concentrations on the (1 1 1) surface of cubic ZrO_2 on the assumption that one S group can bond to three Zr atoms.

An area of 1.0819 × 1.0819 nm on the (1 1 1) surface of pure cubic ZrO_2 (a = 5.10 Å), which contains 16 Zr atoms, was adopted to calculate the surface concentration of S. The one-monolayer S concentration over the (1 1 1) surface of pure cubic ZrO_2 was estimated to be 5.0 nm^{-2}, which was in good agreement with the results of Li et al. [60]. Similar results were also reported by Kantcheva [46]. Taking into account the surface area data described in Table 1, the S concentrations are estimated to be 2.1 nm^{-2} for the SZC sample with 1 wt.% S and 4.3 nm^{-2} for the 2 wt.% S sample. For SZC samples, Co species entered the lattice of cubic zirconia, and a Zr/Co mole ratio of 9 was employed. In this case, one-ninth of the Zr sites are replaced by Co at the surface and in the bulk. Hence, the real single monolayer concentration of S in the Zr–Co cubic phase should be 4.5 nm^{-2}. This result suggests that the surface of SZC samples with 2 wt.% S would be closely covered by one-monolayer of S.

When the S content was increased to 3 wt.%, the calculated S concentration was 5.3 nm^{-2}. As a result, not enough Zr sites were available for the adsorption of S species on the SZC samples, and more than one S monolayer would occupy Co sites. The broadening of XRD peaks (Fig. 3a) and the formation of Co_3O_4 in the 3 wt.% S SZC (Fig. 6, Table 6) clearly demonstrated a reconstruction. In other words, Co species in the SZC samples with 3 wt.% S were eliminated from the Zr–Co solution and occupied Brønsted acid sites. Such a transformation would decrease the number of Brønsted acid sites of SZC with 3 wt.% S compared to the SZC with 2 wt.% S (Figs. 1a and 2a).

4.2. Role of acid sites

As described in Table 1, PdSZC and PdCoSZ possessed almost the same BET surface area, which does not account for their significant difference in NO_x reduction activity. The state of Pd species had a significant influence on the activity of low-loading Pd catalysts supported on acidic materials (such as sulfated zirconia), which strongly depended on the metal loading and the acidity of the supporting material [27]. In our case, the same amount of Pd was loaded onto SZC and CoSZ, which also does not result in any

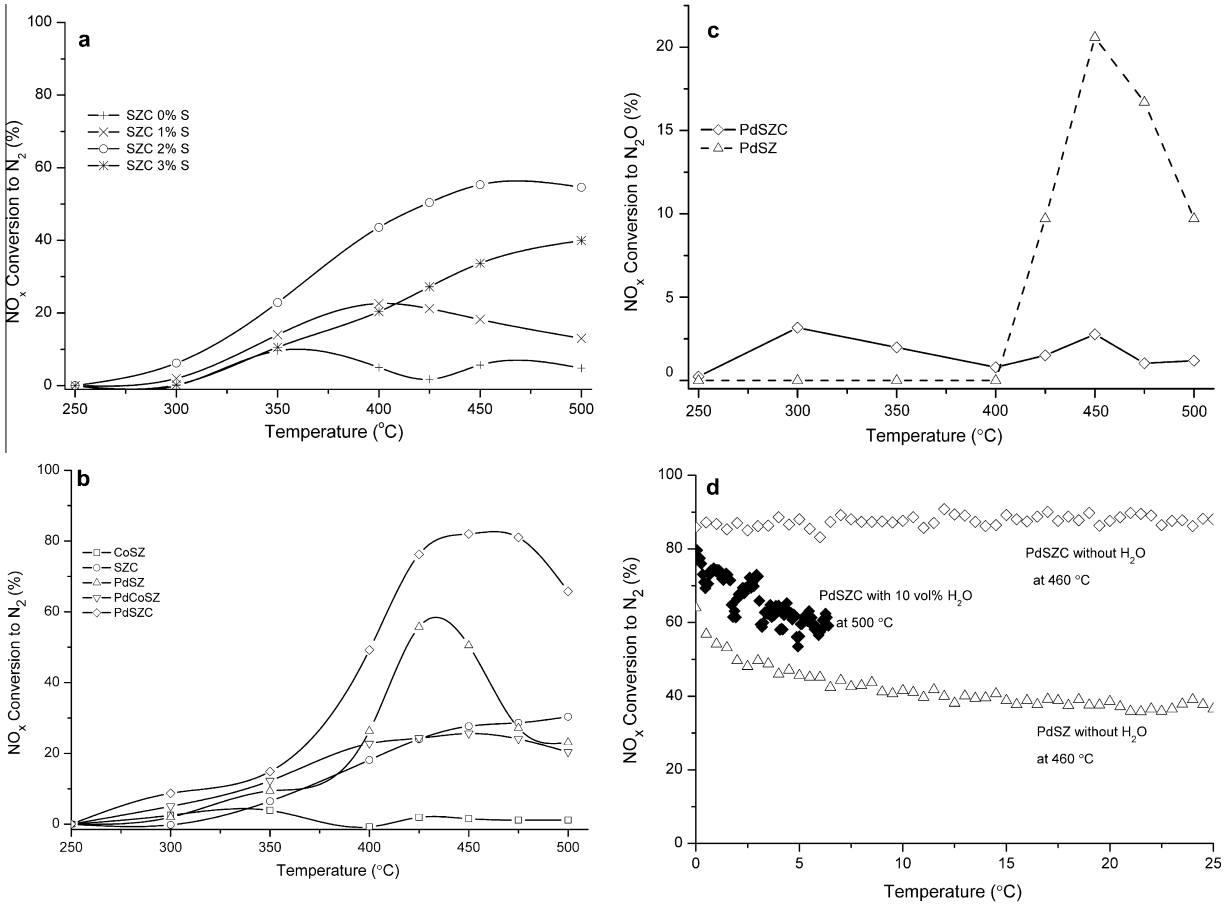

Fig. 8. (a) NO_x conversion to N_2 over SZC samples with different S content; (b) NO_x conversion to N_2 over CoSZ, SZC, PdSZ, PdCoSZ, and PdSZC (all sample with 2 wt.% S loading); (c) NO_x conversion to N_2O over PdSZ and PdSZC; (d) durability of PdSZ and PdSZC for CH_4-SCR without water at 460 °C and with water at 500 °C. Reaction conditions: 1500 ppm CH_4, 500 ppm NO, 7.5 vol.% O_2, balanced by N_2, 200 ml min^{-1} total flow rate, and GHSV = 3600 h^{-1} in (a) and 10,000 h^{-1} in (b–d).

difference in NO_x reduction. Consequently, the acid sites on these materials play a crucial role during CH_4-SCR.

The pyridine adsorption results indicated that Lewis and Brønsted acid sites coexisted on the surface of PdSZC and PdCoSZ (Fig. 1). The appearance of a peak at 1541 cm^{-1} was attributed to the presence of Brønsted acid sites, while the peaks at 1444 and 1439 cm^{-1} were attributed to the Lewis sites. These two peaks exhibited almost the same intensities on the surfaces of the CoSZ, SZC, PdSZC, and PdCoSZ samples. The four samples possessed different activities for NO_x reduction, demonstrating the minor role of Lewis acid sites in CH_4-SCR.

As shown in Fig. 1b, the number of Brønsted acid sites on SZC decreased noticeably after Pd was loaded, while little change was observed for Pd-loaded CoSZ. These results strongly suggest that Brønsted acid sites play a key role in anchoring Pd to form active species. TPR results (Fig. 9) further confirm that Pd species are mainly present as highly dispersed Pd^{2+} on SZC, whereas PdO species were predominant on CoSZ. Considering that the PdO species are active during the combustion of methane, the dispersed Pd^{2+} was attributed to the selective reduction of NO_x to N_2 [27,41]. It is thus reasonable to conclude that PdSZC possesses much higher activity for CH_4-SCR than PdCoSZ.

4.3. Possible mechanism for the introduction of Co into zirconia by different methods

Based on the above results, we can conclude that the transition metal Co^{2+} was successfully introduced into zirconia with little change in Brønsted acid sites. The preparation process of solid acid materials via the new and conventional method is proposed in Scheme 1.

In the direct sulfation method, a solid solution of Zr–Co oxides is formed by the co-precipitation of Zr and Co precursors, during which Co enters the lattice of cubic zirconia by isomorphous substitution of Zr. When the S content is below 3 wt.%, the sulfation does not induce phase transformation of cubic zirconia to a tetragonal structure, indicating that the Zr–Co solid solution is not destroyed in this case. As a result, a large number of Brønsted acid sites remain on the surfaces of the SZC samples, providing sufficient sites for further introduction of Pd^{2+} and subsequent catalytic reaction, and relating closely to the high performance of PdSZC for CH_4-SCR. In the traditional impregnation method, Co is preferentially adsorbed onto the Brønsted acid sites of SZ, leading to obvious decreases in the availability of Brønsted acid sites for Pd anchoring in the form of Pd^{2+}. The activity of PdCoSZ for NO_x reduction is thus reduced.

5. Conclusions

This study successfully introduced the transition metal Co^{2+} into a solid acid by the direct sulfation of Zr–Co hydroxides, with little change in the availability of Brønsted acid sites. XRD, Raman, and XAS analyses demonstrated that zirconia in SZC was present in the cubic phase. Furthermore, Co *K*-edge XAS provided direct evidence of Co entrance into the lattice of cubic zirconia to form a substitutional solid solution. As a result, sufficient Brønsted acid sites remained available for the introduction of Pd^{2+} and catalytic reaction, which accounts for the high activity of PdSZC during

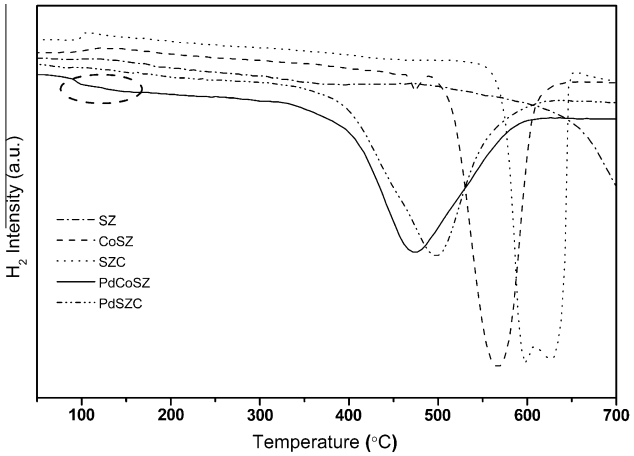

Fig. 9. H_2-TPR for SZ, CoSZ, SZC, PdCoSZ, and PdSZC (all samples with 2 wt.% S). The procedures were as follows: (1) pretreatment of 0.15-g sample in O_2 at 500 °C for 1 h; (2) cooling down to room temperature purging with Ar for 1 h; (3) heating at a ramp of 10 °C/min from 50 to 700 °C in a H_2/Ar (4.79 vol.%) flow of 40 ml/min and recording mass signals of H_2 (m/z = 2), H_2O (m/z = 18), CO_2 (m/z = 44), SO_2 (m/z = 64), and H_2S (m/z = 34) simultaneously.

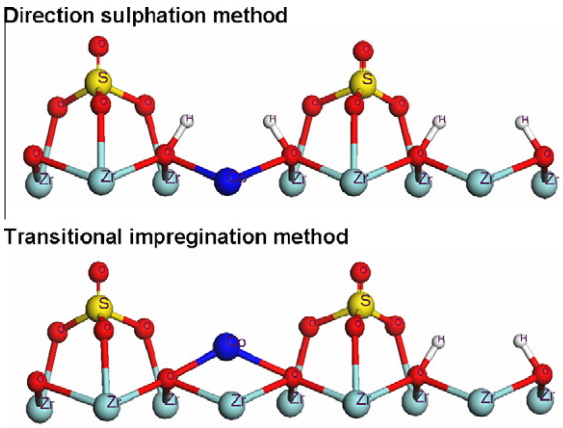

Scheme 1. Possible mechanism of introduction of Co into zirconia by different methods.

CH_4-SCR. As a new and simple approach, the direct sulfation method provides significant advantages for the design of catalysts that require Brønsted acid sites and for further introduction of other active components.

Acknowledgment

This work was financially supported by the National Natural Science Foundation of China (50921064, 10735090, and 20973193).

References

[1] M. Hino, S. Kobayashi, K. Arata, J. Am. Chem. Soc. 101 (1979) 6439.
[2] K. Arata, Adv. Catal. 37 (1990) 165.
[3] A. Corma, Chem. Rev. 95 (1995) 559.
[4] G. Magnacca, G. Cerrato, C. Morterra, M. Signoretto, F. Somma, F. Pinna, Chem. Mater. 15 (2003) 675.
[5] X.M. Song, A. Sayari, Catal. Rev. Sci. Eng. 38 (1996) 329.
[6] J. Deutsch, H.A. Prescott, D. Müller, E. Kemnitz, H. Lieske, J. Catal. 231 (2005) 269.
[7] M.V. Luzgin, K. Thomas, J. Gestel, J.P. Gilson, A.G. Stepanov, J. Catal. 223 (2004) 290.
[8] J.H. Zhang, J.B. Nicholas, J.F. Haw, Angew. Chem. Int. Ed. 39 (2000) 3302.
[9] X.B. Li, K. Nagaoka, L.J. Simon, R. Olindo, J.A. Lercher, A. Hoffmann, J. Sauer, J. Am. Chem. Soc. 127 (2005) 16159.
[10] M. Haouas, S. Walspurger, F. Taulelle, J. Sommer, J. Am. Chem. Soc. 126 (2004) 599.
[11] B.M. Reddy, M.K. Patil, Chem. Rev. 109 (2009) 2185.
[12] X.B. Li, K. Nagaoka, R. Olindo, J.A. Lercher, J. Catal. 238 (2006) 39.
[13] M.A. Al-Daous, A. Stein, Chem. Mater. 15 (2003) 2638.
[14] J.A. Navio, G. Colón, P.J. Sánchez-Soto, M. Macias, Chem. Mater. 9 (1997) 1256.
[15] R. Srinivasan, T.R. Watkins, C.R. Hubbard, B.H. Davis, Chem. Mater. 7 (1995) 725.
[16] F. Haase, J. Sauer, J. Am. Chem. Soc. 120 (1998) 13503.
[17] J.F. Haw, J.H. Zhang, K. Shimizu, T.N. Venkatraman, D-P. Luigi, W.G. Song, D.H. Barich, J.B. Nicholas, J. Am. Chem. Soc. 122 (2000) 12561.
[18] A.G. Stepanov, M.V. Luzgin, A.V. Krasnoslobodtsev, V.P. Shmachkova, N.S. Kotsarenko, Angew. Chem. Int. Ed. 39 (2000) 3658.
[19] N. Li, A.Q. Wang, M.Y. Zheng, X.D. Wang, R.H. Cheng, T. Zhang, J. Catal. 225 (2004) 307.
[20] N. Li, A.Q. Wang, J.W. Tang, X.D. Wang, D.B. Liang, T. Zhang, Appl. Catal. B 43 (2003) 195.
[21] B.S. Klose, F.C. Jentoft, R. Schlögl, I.R. Subbotina, V.B. Kazansky, Langmuir 21 (2005) 10654.
[22] F.C. Jentoft, A. Hahn, J. Kröhnert, G. Lorenz, R.E. Jentoft, T. Ressler, U. Wild, R. Schlögl, C. Häßner, K. Köhler, J. Catal. 224 (2004) 124.
[23] W.M. Hua, Y.D. Xia, Y.H. Yue, Z. Gao, J. Catal. 196 (2000) 104.
[24] T. Yamamoto, T. Tanaka, S. Takenaka, S. Yoshida, T. Onari, Y. Takahashi, T. Kosaka, S. Hasegawa, J. Phys. Chem. B 103 (1999) 2385.
[25] C.-Y. Hsu, C.R. Heimbuch, C.T. Armes, B.C. Gates, J. Chem. Soc. Chem. Commun. 22 (1992) 1645.
[26] T. Kurosaka, H. Matsuhashi, K. Arata, J. Catal. 179 (1998) 28.
[27] A. Ali, W. Alvarez, C.J. Loughran, D.E. Resasco, Appl. Catal. B 14 (1997) 13.
[28] A.W. Aylor, L.J. Lobree, J.A. Reimer, A.T. Bell, J. Catal. 172 (1997) 453.
[29] M.V. Luzgin, V.A. Rogov, S.S. Arzumanov, A.V. Toktarev, A.G. Stepanov, V.N. Parmon, Angew. Chem. Int. Ed. 47 (2008) 4559.
[30] M.H. Groothaert, P.J. Smeets, B.F. Sels, P.A. Jacobs, R.A. Schoonheydt, J. Am. Chem. Soc. 127 (2005) 1394.
[31] V.R. Choudhary, A.K. Kinage, T.V. Choudhary, Science 275 (1997) 1286.
[32] N. Li, A.Q. Wang, J.W. Tang, X.D. Wang, D.B. Liang, T. Zhang, Appl. Catal. B 43 (2003) 201.
[33] Y. Nishizaka, M. Misono, Chem. Lett. (1994) 2237.
[34] Y. Nishizaka, M. Misono, Chem. Lett. (1993) 1295.
[35] L. Ren, T. Zhang, D.B. Liang, C.H. Xu, J.W. Tang, L.W. Lin, Appl. Catal. B 35 (2002) 317.
[36] Y. Li, J.P. Battavio, J.N. Armor, J. Catal. 142 (1993) 561.
[37] Y. Li, J.N. Armor, Appl. Catal. B 3 (1993) L1.
[38] Y. Li, J.N. Armor, Appl. Catal. B 1 (1992) L31.
[39] B. Mirkelamoglu, U.S. Ozkan, Appl. Catal. B 96 (2010) 421.
[40] C. Quincoces, A. Ruber, P. Araya, D. Gazzoli, M.G. González, Catal. Commun. 10 (2008) 74.
[41] A. Ruber, C. Quincoces, A.S. Mamede, D. Gazzoli, C. Cabello, M.G. González, Catal. Commun. 9 (2008) 1096.
[42] R. Marques, L. Mazri, S. Da Costa, F. Delacroix, G. Djéga-Mariadassou, P. Da Costa, Catal. Today 137 (2008) 179.
[43] R. Marques, L. Mazri, S. Da Costa, F. Delacroix, G. Djéga-Mariadassou, P. Da Costa, Catal. Today 137 (2008) 185.
[44] T.V. Myronyuk, S.N. Orlyk, Catal. Today 119 (2007) 152.
[45] L.F. Córdoba, W.M.H. Sachtler, Appl. Catal. B 56 (2005) 269.
[46] M. Kantcheva, A.S. Vakkasoglu, J. Catal. 223 (2004) 364.
[47] M. Kantcheva, A.S. Vakkasoglu, J. Catal. 223 (2004) 352.
[48] http://cars9.uchicago.edu/ifeffit/.
[49] J.J. Rehr, R.C. Albers, Rev. Mod. Phys. 72 (2000) 621.
[50] A.C. Larson, R.B. Von Dreele, General Structure Analysis System (GSAS), LosAlamos National Laboratory Report LAUR, 2004, p. 86.
[51] C. Li, P.C. Stair, Catal. Lett. 36 (1996) 119.
[52] D. Grandjean, A.M. Beale, A.V. Petukhov, B.M. Weckhuysen, J. Am. Chem. Soc. 127 (2005) 14454.
[53] T. Xingfu, L. Junhua, S. Liang, H. Jiming, Appl. Catal B 99 (2010) 156.
[54] E.M. Holmgreen, M.M. Yung, U.S. Ozkan, Appl. Catal. B 74 (2007) 73.
[55] J.A.Z. Pieterse, S. Booneveld, Appl. Catal. B 73 (2007) 327.
[56] X. Xia, R. Oldman, R. Catlow, Chem. Mater. 21 (2009) 3576.
[57] A. Christensen, E.A. Carter, Phys. Rev. B 58 (1998) 8050.
[58] M.A. Ecormier, K. Wilson, A.F. Lee, J. Catal. 215 (2003) 57.
[59] N. Katada, J. Endo, K. Notsu, N. Yasunobu, N. Naito, M. Niwa, J. Phys. Chem. B 104 (2000) 10321.
[60] X.B. Li, K. Nagaoka, L.J. Simon, J.A. Lercher, S. Wrabetz, F.C. Jentoft, C. Breitkopf, S. Matysik, H. Papp, J. Catal. 230 (2005) 214.